Modeling the Effect of Residual Stress on the Ductile Fracture Behavior of an Aluminum Alloy 5083-H116

Xiaosheng Gao[1,*], Jun Zhou[1], Matthew Hayden[2]

[1] Department of Mechanical Engineering, The University of Akron, Akron, OH 44325, USA
[2] Alloy Development and Mechanics Branch, Naval Surface Warfare Center, West Bethesda, MD 20817, USA
* Corresponding author: xgao@uakron.edu

Abstract The influence of residual stress on the ductile fracture behavior of an aluminum alloy 5083-H116 is investigated in this study through a series of experiments and finite element analyses. A recently developed stress state dependent I_1-J_2-J_3 plasticity model, is implemented to describe the plastic response of this material. A ductile failure criterion based on the damage parameter defined in terms of the accumulative plastic strain as a function of the stress triaxiality and Lode angle is established. The calibrated I_1-J_2-J_3 plasticity model and ductile failure model are utilized to study the residual stress effect on ductile fracture resistance. A local out-of-plane compression approach is employed to generate residual stress fields in the compact tension specimens. Fracture tests of C(T) specimens having zero, positive and negative residual stresses are conducted. The numerical results, such as load-displacement curves and crack front profiles, are compared with experimental measurements and good agreements are observed. Both experimental and finite element results show significant effect of residual stress on ductile fracture resistance.

Keywords Ductile fracture, Plasticity, Damage accumulation, Stress triaxiality, Lode angle

1. Introduction

Residual stresses in the engineering structures are generated from forming, welding, assembling, heat treatment etc., which play an important role in either increasing or decreasing the fracture resistance. The compressive residual stress generally improves the fracture toughness, while the tensile residual stress can detrimentally reduce the loading capacity of the structure. This is usually attribute to the additional crack driving force and change of the crack front constraint [1]. To quantify the effect of residual stress on fracture toughness, it is necessary to introduce well characterized and reproducible residual stress fields into fracture specimens. There are plenty of literatures on residual stress generation techniques, which can either be mechanical or thermal process. Almer et al. [2] deformed large tensile specimens and cut the gauge sections to produce C(T) specimens. Meith et al. [3] applied local compression to the sides of fracture specimens. Because of the strain incompatibility between elastic and plastic region caused by the permanent plastic deformation, the residual stress field can be generated in the specimen. This local out-of-plane compression (LOPC) approach is further explored by Mahmoudi et al. [4], who ran a series experiments and finite element analyses to examine how the position of compression tools influences the residual stress distribution in the specimen.

In this study, we employ the LOPC approach and use two pairs of compression punches to generate various residual stress fields in C(T) specimens. To model these specimens, a recently developed I_1-J_2-J_3 dependent plasticity model is used to describe the plastic response of the material, an aluminum alloy 5083-H116. The residual stress field is quantified by conducting finite element simulation of the out-of-plane compression process. After the residual stress field is generated, fracture tests of C(T) specimens having positive and negative residual stresses are conducted and simulated numerically. A damage parameter is defined as a weighted integral with respect to the effective strain, where the integrand is the reciprocal of the effective failure strain as a function of the stress triaxiality and the Lode angle. Fracture is assumed to have initiated at a material point once the failure criterion is reached. A mesh-independent, post-initiation material degradation model based on an effective plastic displacement is adopted before the element is removed. The

numerical results, such as load-displacement curves and crack front profile, are compared with the experimental measurements and good agreements are observed.

2. Plasticity and Fracture Models

Gao et al. [5] and Zhou et al. [6] have demonstrated that the plastic response of the aluminum alloy 5083-H116 considered in this study can be described by an I_1-J_2-J_3 dependent plasticity model with the yield function and flow potential given by

$$F = c_1(a_1 I_1^6 + 27J_2^3 + b_1 J_3^2)^{1/6}; \qquad G = c_2(a_2 I_1^6 + 27J_2^3 + b_2 J_3^2)^{1/6} \tag{1}$$

where a_i and b_i are material constants, $c_i = 1/(a_i+4b_i/729+1)^{-1/6}$, I_1 is the first invariant of the stress tensor, and J_2 and J_3 are the second and third invariants of the stress deviator tensor respectively. The equivalent stress-strain relation (true stress vs. logarithm strain) is obtained by the uniaxial tension test, which can be described by a power-law hardening relation

$$\begin{aligned} \varepsilon &= \frac{\sigma}{E} && \text{when } \ \sigma \le \sigma_0 \\ \varepsilon &= \frac{\sigma_0}{E}\left(\frac{\sigma}{\sigma_0}\right)^{1/N} && \text{when } \ \sigma > \sigma_0 \end{aligned} \tag{2}$$

with E = 68.4 GPa, σ_0 = 198.6 MPa, ν = 0.3, and N = 0.155. Other material constants are calibrated using experimental data obtained from uniaxial tension, compression, pure torsion and combined torsion-tension tests. The calibrated values are $a_1 = a_2 = 0$, b_1 = -60.75 and b_2 = -50.

The cumulative strain damage models assume damage toward eventual fracture is due to the plastic deformation history and the equivalent fracture strain depends on the stress state subjected by the material. Here a damage parameter, D, is introduced and given by

$$D = \int_0^{\bar{\varepsilon}^p} \frac{d\bar{\varepsilon}^p}{\varepsilon_f(T^*, \xi)} \tag{3}$$

with ε_f being the failure strain depending on the stress triaxiality ratio and the Lode parameter ξ defined as

$$T^* = \frac{\sigma_h}{\sigma_e}, \qquad \xi = \frac{27J_3}{2\sigma_e^{\,3}} \tag{4}$$

where ξ is related to the Lode angle, θ, through $\xi = \cos(3\theta+\pi/2)$. Under proportional loading and if T^* and ξ remain unchanged during the loading history, when the equivalent plastic strain, $\bar{\varepsilon}^p$, reaches the critical value ε_f, D will equal to unit. For general cases, when the cumulative damage according to Eq. (3) reaches one, ductile failure is said to have happened.

When ξ is a constant, ε_f becomes a function of T^* only. It is well documented that the ductility of metals increases when the material is subjected to hydrostatic pressure. Here an exponentially

decaying function having the same form as the Johnson-Cook fracture model [7] is used to describe the dependency of ε_f on T^*

$$\varepsilon_f^{\xi=const.} = [A + B\exp(C \cdot T^*)] \tag{5}$$

where A, B and C are material constants to be calibrated using experimental data.

The Lode angle distinguishes the deviatoric stress state and it is mathematically convenient to use the parameter ξ defined in Eq. (4), whose range is from -1 to 1, to quantify the Lode angle. Wilkins et al. [8] was first to introduce the effect of Lode angle on ductile fracture, where the function $\varepsilon_f(T^*, \xi)$ was taken to be symmetric with respect to ξ. Here we follow Xue and Wierzbicki [9] and assume $\varepsilon_f(T^*, \xi)$ take the following form

$$\varepsilon_f(T^*, \xi) = \varepsilon_f^{\xi=1}(T^*) - (\varepsilon_f^{\xi=1}(T^*) - \varepsilon_f^{\xi=0}(T^*))[1 - (1 - |\xi|^n)^{1/n}] \tag{6}$$

where a symmetric function of ξ is used to interpolate the value of ε_f between two bounding values $\varepsilon_f^{\xi=1}$ and $\varepsilon_f^{\xi=0}$. The two bounding curves, $\varepsilon_f^{\xi=1}(T^*)$ and $\varepsilon_f^{\xi=0}(T^*)$ given by Eq. (7), can be calibrated by conducting simple mechanical tests: ξ =1 for notched, round tensile specimens and ξ =0 for flat-grooved plates under tension and the thin-walled torsion specimen. Calibration of parameter n requires performing additional tests using specimens having ξ values between zero and one, which can be done by conducting combined torsion-tension tests of thin-walled cylindrical specimens.

$$\varepsilon_f^{\xi=1} = [A_1 + B_1\exp(C_1 \cdot T^*)]; \quad \varepsilon_f^{\xi=0} = [A_2 + B_2\exp(C_2 \cdot T^*)] \tag{7}$$

The calibrated material parameters are A_1 =0, B_1=0.85, C_1=-1.9, A_2 =0, B_2=0.64, C_2=-1.9, and n = 1.31. The 3D failure locus expressed in terms of ε_f as a function of ξ and T^* is shown in Figure 1.

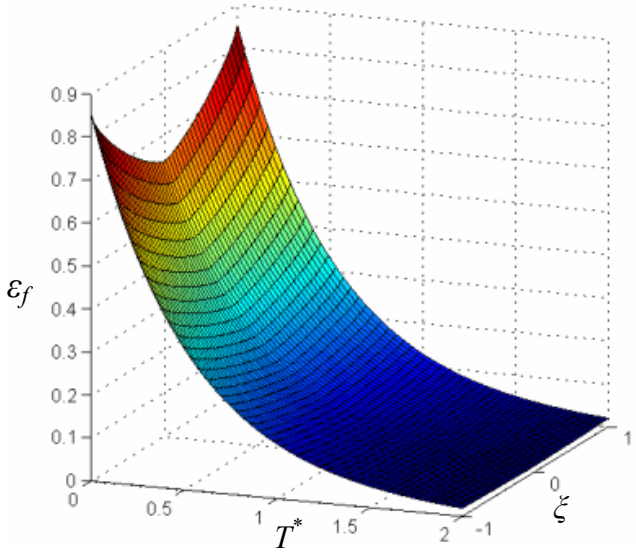

Figure 1. 3D plot of the failure locus

Fracture is assumed to have initiated at a material point once the failure criterion is reached. The post-initiation softening process needs to be considered in order to model crack propagation. As illustrated by Li et al. [10], because the finite element has a finite size, additional work is needed to

propagate the crack through the element, i.e., the element gradually loses its strength as crack grows through it. A mesh-independent, post-initiation material degradation model based on an effective plastic displacement (u_f) is available in ABAQUS [11] and is adopted in this study. The element is removed when it is fully degraded (stresses being reduced to zero).

3. Fracture Specimen and Residual Stress Generation

The 1/2T C(T) specimens (thickness: 12.7 mm) are used in the fracture tests. The specific design utilized in this study is modified from the standard design specified by ASTM-E1820 as a means of applying controlled residual stresses. The aim is to introduce residual stresses into the C(T) specimen by compressing the two faces with cylindrical punches to a specified displacement to produce a pair of permanent depressions on both faces of the specimen. From the analyses performed by Mahmoudi et al. [4], the size and position of the punching tools have strong influence on the magnitude and distribution of the residual stress field. Thus one can tailor the residual stress field at the crack tip by varying the position of the set of depressions relative to the crack tip.

A series finite element analyses are conducted first to determine the diameter, applied displacement, and locations of each depression, in order to obtain larger residual stress influenced region. From these analyses, the 8.89 mm punch radius is selected and the punch position is chosen to be $\delta_x / R = 1$ and -1, $\delta_y / R = 1.2$, where δ_x and δ_y are the distances from the punch center to the crack tip parallel and normal to the crack growth direction respectively and R is the radius of the punch.

With the aid of the above analyses, fixtures were designed for use in side compression. The specimen is sandwiched between two guide plates. The guide plates are aligned with the specimen by threading two pins through one guide plate, the pin loading holes of the specimen, and through the other guide plate. These guide pins ensure consistency in locating the side compression indentations between specimens. Two side compression punches (one on either side of the crack plane) are placed in the top guide plate and two mating punches are placed in the bottom guide plate. Once assembled, the compression force is applied to the top punches while the bottom punches remain fixed. Sets of fixtures were designed and machined for both the δ_x/R = 1 and δ_x/R = -1 configurations (δ_y/R = 1.2). Figure 2 illustrate the schematic of side compression fixture.

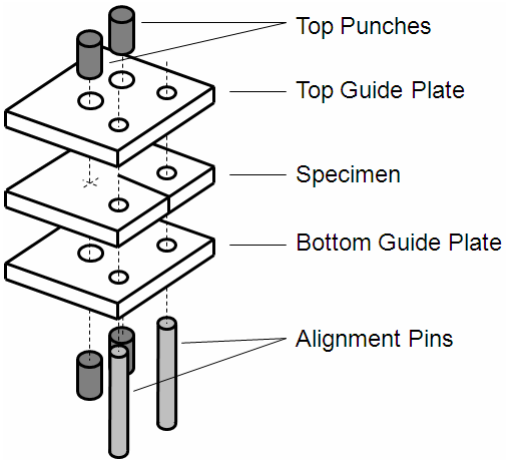

Figure 2. Schematic of side compression fixture

4. Experimental and Numerical Results

4.1. C(T) specimens without residual stress

The plane-sided C(T) specimen is considered first. Due to symmetry of the geometry and the boundary conditions, only a quarter of the specimen is meshed. The element size along the crack path is 0.254 mm in all three directions. The eight-node, isoparametric, brick elements with reduced integration are used in the analysis. Figure 3 compares the predicted crack profile with the fracture surface of the broken specimen and the agreement is very good. A “V” shape crack profile, seen in both test and simulation results, shows strong crack tunneling effect. This is due to the variation of the constraint in the thickness direction, where the plane stress prevails at the free surface and the plane strain condition prevails in the center. Figure 3 (b) displays the stress triaxiality contour on the crack plane, showing the stress triaxiality decreases from the mid-plane to the free surface. The computed and measured load vs. load line displacement curves of the plane-sided C(T) specimen are compared in Figure 4. Good agreement is observed before fracture initiation and at the early stage of crack growth.

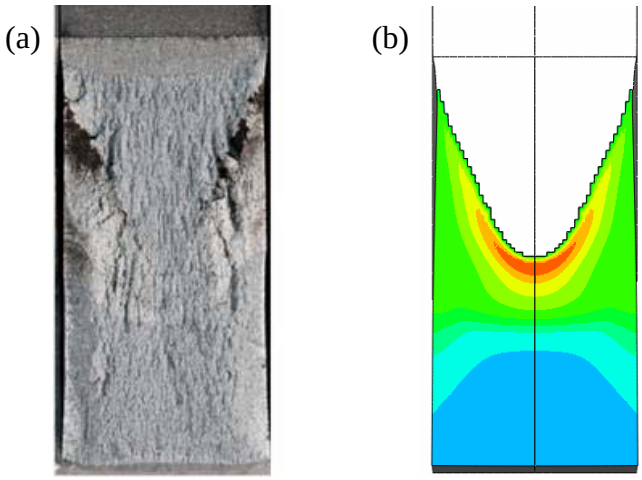

Figure 3. Fracture surface and stress triaxiality distribution in the plane-sided C(T) specimen

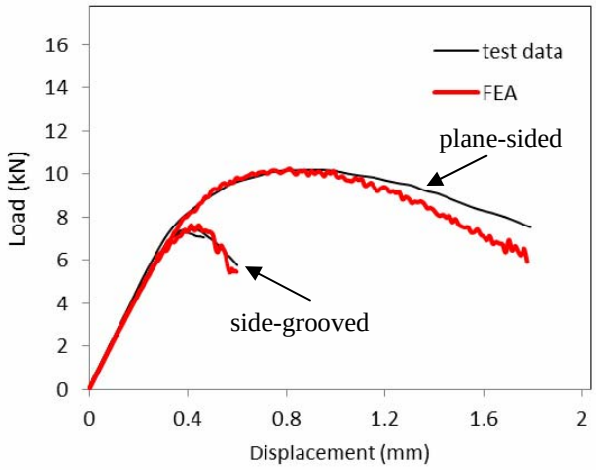

Figure 4. Comparison of the load-displacement curves for plane-sided and side-grooved specimens

In order to promote plane strain constraint along the crack front and obtain more uniform though thickness crack growth, the C(T) specimens are side-grooved by 20% of the thickness (10% each side). Consequently, a quarter-symmetric finite element model is generated for the side-grooved specimen, in which the same element type and size are used as those for the plane-sided specimen. With the side grooves, the constraint level is significantly raised close to specimen edges and as a result, more uniform crack growth (less tunneling) is observed. Figure 5(a) compares the predicted crack profile with the crack surface of the broken specimen. Figure 5(b) shows stress triaxiality becomes almost uniform through specimen thickness due to the side grooves. Because the constraint level is raised by the side grooves, fracture becomes easier, resulting in a lower load carrying capacity by the specimen. As shown in Figure 4 the load carrying capacity of the C(T) specimen is significantly reduced by the side grooves.

In conducting the experiments, the test was stopped after some amount of crack extension and the specimen was broken by fatigue loading. The post fatigue marks were used to determine the amount of crack growth. Due to the non-uniform crack growth through the specimen thickness, a nine-point

average was used to determine the crack length. We compare the model predicted crack growth with experimental measurements at the same applied load levels and find very good agreements between the two. For examples, C(T)-17 has crack extensions of 6.81 mm (measured from post fatigue marks) when the test was stopped. The finite element analyses predict the amount of crack extension of 7.11 mm at the same load level.

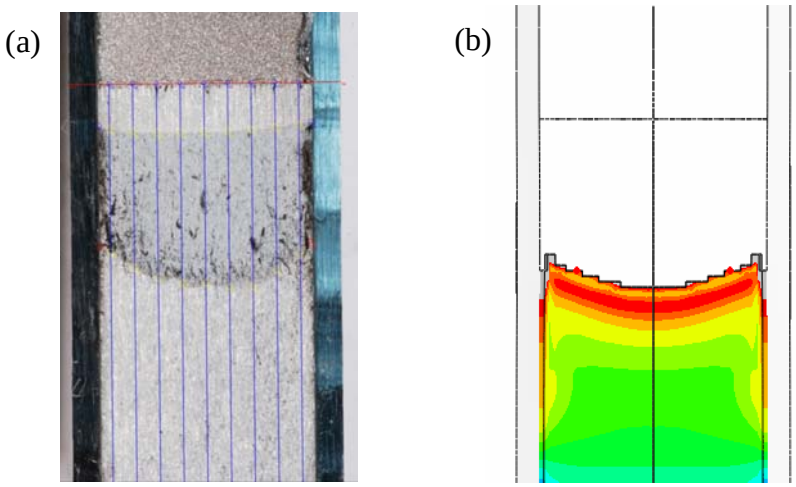

Figure 5. Fracture surface and stress triaxiality distribution in the side-grooved C(T) specimen.

4.2. Fracture tests with tensile residual stress

The C(T) specimens considered hereafter are all side-grooved. Two levels of compression forces, 182 kN and 220 kN, were used in the experiments to generate tensile residual stresses. The average total indentation depths (after the punches were removed) are 0.083 mm and 0.244 mm for 182 kN and 220 kN respectively. The finite element analyses results in 0.089 mm and 0.259 mm total indentation depths for these two cases.

Since the LOPC method creates residual stress field by introducing plastic strain into structure, too much side compression may results in the crack extension. Several methods, such as dye injection and SEM observation of the fracture surface, are used to verify if this has happened. From result of the dye and also SEM observations, the tensile residual side compression does result in crack initiation and growth when 220 kN load was applied. SEM observations also showed clear damage, i.e., inclusions broken and pulled loose from the matrix. However, this was not observed for the 182 kN case.

The simulation results for both cases confirm the experimental observations. Figure 6 shows the crack front region after side compression, suggesting crack does extend about 1.5 mm when 220 kN of compression force is employed, whereas crack extension does not happen when 182 kN compression force is applied. The contours of residual stresses normal to the crack plane for both cases are shown in Figure 6. The high positive residual stress is confined in a small region close to the crack tip, within about 1.3 mm from the crack tip, and the residual stress distribution is fairly uniform along the crack front except in the region close to the free surface.

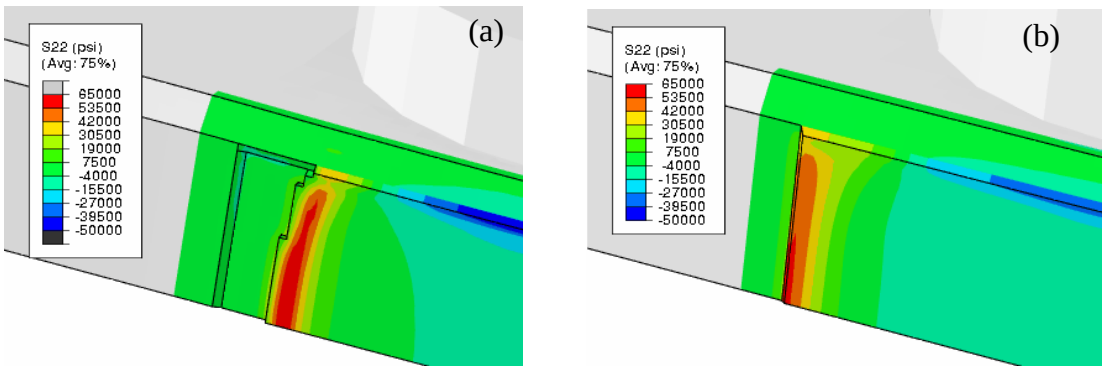

Figure 6. Contour plots of the residual stress normal to the crack plane: (a) 220 kN side-compression, (b) 182 kN side-compression (stress unit in contour plots: psi)

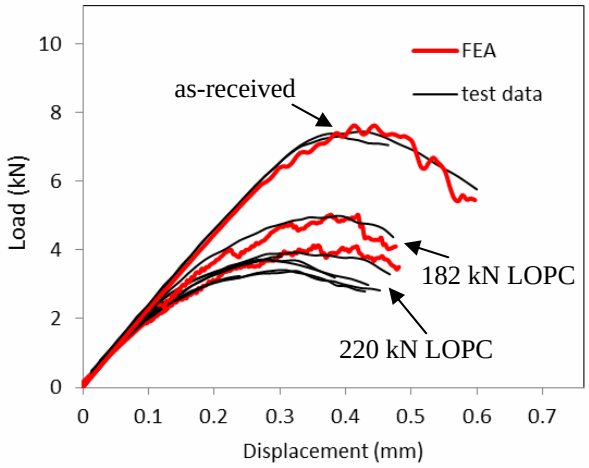

Figure 7. Comparisons of the computed and measured load-displacement curves for C(T) specimen without residual stress and with tensile residual stress

After the residual stress fields have been generated in the specimens, finite element analyses of the compact tension tests of these specimens are carried out. Figure 7 compares the model predicted load-displacement curves with experimental records for the as-received specimen as well as the specimens with tensile residual stress field. The numerical model captures the effect of the tensile residual stress on the fracture resistance. The existence of tensile residual stress drastically reduces the fracture resistance and lowers the specimen's load carrying capacity. After crack grows away from the residual stress influence area, the features of crack growth become similar to those exhibited by the virgin specimen.

4.3. Fracture tests with compressive residual stress

When side-compression is applied behind the crack tip, crack will close and the crack surfaces will contact each other. In finite element analysis, to prevent crack surface penetration, a rigid surface is added to the symmetric plane behind the crack tip. The finite element analysis results show that the high compressive residual stress region is at the initial EDM notch (behind the fatigue pre-crack front) and the residual stress distribution is not as uniform as tensile residual stress case, Figure 8(a). Figure 8(b) shows the variation of the residual stress (σ_{22}) with the distance in the crack growth

direction at the mid-plane respectively.

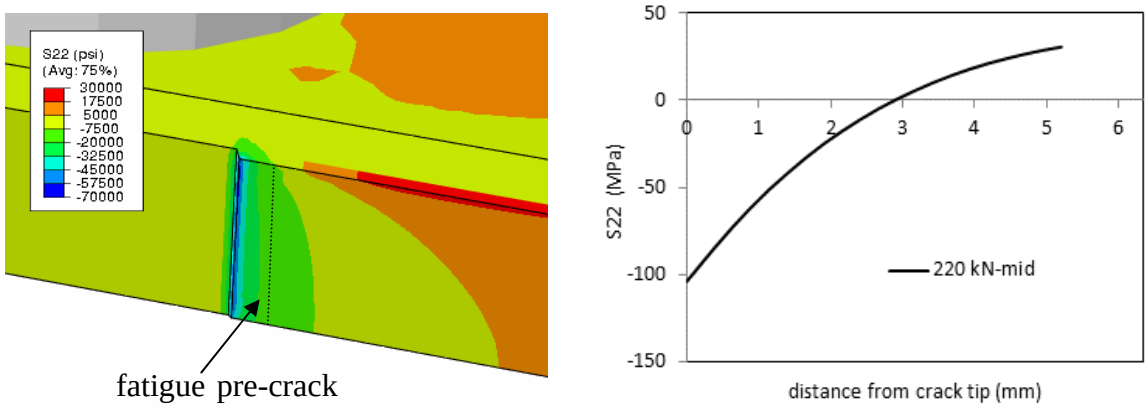

Figure 8. (a) Contour plot of the residual stress normal to the crack plane, (b) variation of the residual stress (σ_{22}) with the distance in the crack growth direction

Compressive residual stresses reduce the constraint level at the crack front region and tend to close the crack, and consequently, increase the fracture resistance. Figure 9 compares the load-displacement curves of the specimen with compressive residual stress field generated by 220 kN side compression with the as received specimen. Included in the figure are also comparisons between the model predictions and the experimental measurements. Again, good agreement is observed.

3. Concluding Remarks

In this study, the residual stress effects on the ductile fracture behavior of the aluminum alloy 5083-H116 are investigated through a series of experiments and finite element analyses. An I_1-J_2-J_3 dependent plasticity model is used to describe the plastic response of the materials and a damage parameter is defined as a weighted integral with respect to the effective strain, where the integrand is the reciprocal of the effective failure strain as a function of the stress triaxiality and the Lode angle. The model parameters are calibrated and validated by comparing the numerical predictions with experimental measurements. To generate residual stress fields in fracture specimens, a local out-of-plane compression approach is adopted and an experimental fixture is designed. The analysis results show that tensile residual stress not only increases the crack driving force but also raises the constraint level in crack tip region, which results in a lower fracture resistance. Compressive residual stress has the opposite effect. The numerical results, such as load-displacement curves and crack front profiles, are compared with experimental measurements and good agreements are observed, suggesting that the numerical model is capable of capturing the residual stress effect on ductile fracture resistance.

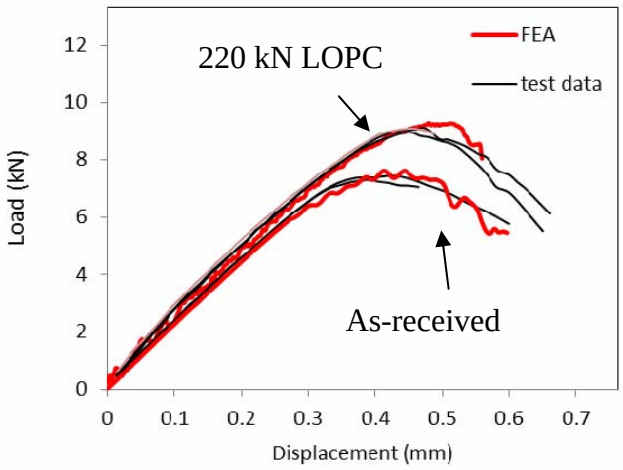

Figure 9. Comparisons of the computed and measured load-displacement curves for C(T) specimen without residual stress and with compressive residual stress.

Acknowledgements

This research is supported by the Ship Structures Committee and the Naval Surface Warfare Center, Carderock Division.

References

[1] T. Panontin, M. Hill, The effect of residual stresses on brittle and ductile fracture initiation predicted by micromechanical models. Int J Fract 82(1996) 317-333.

[2] J. Almer, J. Cohen, R. Winholtz, The effects of residual macrostresses and microstresses on fatigue crack propagation. Metall Mater Trans A 29(1998) 2127-2136.

[3] W. Meith, M. Hill, T. Panontin, Analytical & Experimental Study of Fracture in Bend Specimens Subjected to Local Compression, in: W.G. Reuter, R.S. Piascik (Eds), Fatigue and Fracture Mechanics: 33rd Volume, ASTM STP 1417, Philadelphia, PA, 2003, pp. 426-444.

[4] A. Mahmoudi, C. Truman, D. Smith, Using local out-of-plane compression (LOPC) to study the effects of residual stress on apparent fracture toughness. Eng Fract Mech 75(2008) 1516-1534.

[5] X. Gao, T. Zhang, J. Zhou, S.M. Graham, M. Hayden, C. Roe, On stress-state dependent plasticity modeling: Significance of the hydrostatic stress, the third invariant of stress deviator and the non-associated flow rule. Int J Plas 27(2011) 217-231.

[6] J. Zhou, X. Gao, M. Hayden, J.A. Joyce, Modeling the ductile fracture behavior of an aluminum alloy 5083-H116. Eng Fract Mech 85(2012) 103-116.

[7] G.R. Johnson, W.H. Cook, Fracture characteristics of three metals subjected to various strains, strain rates, temperatures and pressures. Eng Fract Mech 21(1985) 31-48.

[8] M. Wilkins, R. Streit, J. Reaugh, Cumulative-strain-damage model of ductile fracture: simulation and prediction of engineering fracture tests. Technical Report UCRL-53058, Lawrence Livermore National Lab., CA , 1980.

[9] L. Xue, T. Wierzbicki, Ductile Fracture Characterization of Aluminum Alloy 2024-T351 Using Damage Plasticity Theory. Int J Appl Mech 1(2009) 267-304.

[10] Y. Li, T. Wierzbicki, M.A. Sutton, J. Yan, X. Deng, Mixed mode stable tearing of thin sheet AI 6061-T6 specimens: experimental measurements and finite element simulations using a modified Mohr-Coulomb fracture criterion. Int J Fract 168(2011) 53-71.

[11] SIMULIA, ABAQUS User's Manual (version 6.9), Providence, RI, 2008.